Materials Today Communications 33 (2022) 105025

Contents lists available at ScienceDirect

Materials Today Communications

journal homepage: www.elsevier.com/locate/mtcomm

Defect induced the surface enhanced Raman scattering of MoO_{3-x} thin films by thermal treatment

Qiankun Huang [a], Qingyou Liu [b], Xiao Li [c], Ruijin Hong [a,*], Chunxian Tao [a], Qi Wang [a], Hui Lin [a], Zhaoxia Han [a], Dawei Zhang [a]

[a] Engineering Research Center of Optical Instrument and System, Ministry of Education and Shanghai Key Lab of Modern Optical System, University of Shanghai for Science and Technology, No.516 Jungong Road, Shanghai 200093, China
[b] Key Laboratory of High-temperature and High-pressure Study of the Earth's Interior, Institute of Geochemistry, Chinese Academy of Sciences, Guiyang 550081, China
[c] Department of Physics, Beijing Technology and Business University, Beijing 100048, China

ARTICLE INFO

Keywords:
MoO_{3-x}
SERS
Thermal treatment
Oxygen defects
FDTD

ABSTRACT

In this paper, we successfully prepared MoO_{3-x} films by magnetron sputtering and thermal treatment. The samples annealed at different temperatures were analyzed by atomic force microscopy, scanning electron microscopy, X-ray diffraction, and X-ray photoelectron spectroscopy, respectively. Compared to as-deposited sample, the thermal treatment has the effects of enhancing localized surface plasmon resonance and Raman scattering intensity, improving the uniformity and stability of Raman signals, and reducing the detection limit for dye methylene blue as low as 5×10^{-7} mol/L. In addition, the simulation results of finite-difference-time-domain confirm that the electric field enhancement effect exists in the defect state metal oxide SERS substrate.

1. Introduction

As a powerful and widely applied analytical technique, surface enhanced Raman spectroscopy (SERS) analysis has become a highly sensitive and non-destructive detection method in biological and chemical analytical fields. It is widely used in medical diagnosis treatment, environmental monitoring, food safety, fingerprint recognition and other fields [1–4]. At present, SERS substrates are basically limited to traditional noble metals [5], which contain a large number of free electrons [6], and their plasmon resonance frequency are basically consistent with the excitation wavelength of Raman spectroscopy commonly used in experiments, thus these metals have strong electromagnetic enhancement [7,8]. However, the preparation of traditional noble metal SERS substrates requires complex and special preparation technology, and suffers from disadvantages such as poor stability, high cost, and low biocompatibility [9,10], which inevitably limit their practical applications. In order to find a more efficient and stable SERS substrate, researchers have gradually turned to metal oxide SERS substrate materials. Compared with traditional noble metals, metal oxide SERS substrates have a series of advantages such as high stability, low cost, high SERS uniformity and good biocompatibility [11–13], but the Raman enhancement effect is poor, the electromagnetic enhancement factors (EFs) are weak (only 10^2–10^3), and the limit of detection (LOD) is low [14], which limit the promotion and application of metal oxide SERS substrates. Therefore, it is of great significance to find efficient metal oxide SERS substrate materials, and these materials also have broad development prospects.

In recent years, researchers had found that by introducing defects and morphology engineering, they had good performance in improving the Raman intensity of metal oxide SERS substrate. For example, sea urchin-like $W_{18}O_{49}$ nanowires based on surface plasmon resonance [15]; highly sensitive and highly stable MoO_2 nanospheres with very high EFs (4.8×10^6) [16] and simple reduction synthesis of highly chemically enhanced MoO_{2-x} nanospheres [17]. Defect engineering is an important means to convert non-SERS active of metal oxides into SERS active substrate, in which oxygen defects can lead to the enhancement of charge transfer resonances in metal oxides [18,19], thus significantly improving Raman enhancement effect.

In this paper, we deposited MoO_{3-x} thin film by magnetron sputtering and then thermal treatment as SERS substrate. By optimizing the thermal treatment temperature to adjust the content of defects in metal oxides, we obtained the suitable SERS substrates. In addition, we use methylene blue (MB) as a probe molecule to study the uniformity and stability of the prepared samples.

* Corresponding author.
E-mail address: rjhong@usst.edu.cn (R. Hong).

https://doi.org/10.1016/j.mtcomm.2022.105025
Received 26 October 2022; Received in revised form 20 November 2022; Accepted 23 November 2022
Available online 24 November 2022

Table 1
Preparation process parameters.

Samples	CFM (sccm)	P (w)	T (s)	Annealing temperature (℃)	Annealing time (min)
S1	40	70	90	0	0
S2	40	70	90	200	30
S3	40	70	90	250	30
S4	40	70	90	300	30

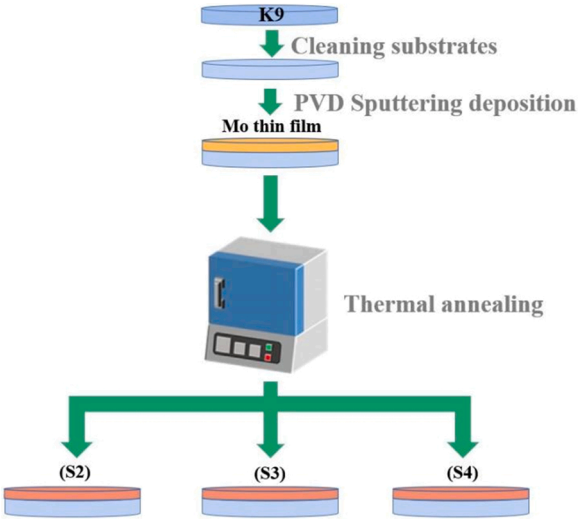

Fig. 1. The schematic diagram of the fabrication process of MoO_{3-x} thin films.

2. Experimental

Molybdenum thin films were deposited on K9 glass substrate by sputtering system from a Mo target (99.99 %) with an argon pressure of 1.0 Pa. Prior to deposition, the K9 substrates were placed sequentially in acetone, ethanol and deionized water for 20 mins by ultrasonic cleaning, and finally dried with a flow of nitrogen. The chamber was pumped to a base pressure of about 1.0×10^{-3} Pa before deposition. The deposited as-deposited samples were respectively placed into a homemade tubular furnace and the MoO_{3-x} films were obtained by thermal treatment under atmospheric conditions. The corresponding preparation process and thermal treatment parameters are shown in Table 1. Meanwhile, the original Mo film was used as a comparison, and the sample preparation process is shown in Fig. 1.

The atomic force microscopy (AFM) (XE-100, ParkSystem) and scanning electron microscopy (SEM) (ZEISS Gemini 300) were employed to characterize the surface morphology of MoO_{3-x} thin films. The crystallinity and phase of the samples were measured by X-ray diffraction (XRD) (Bruker AXS/D8 advanced system, $\lambda = 0.15408$ nm). The absorption spectra of the samples were analyzed using a dual-beam spectrophotometer (Lambda1050, Perkinelmer, USA) with a measurement range of 300–2000 nm and a step size of 2 nm. The composition and valence changes of samples were analyzed by X-ray photoelectron spectroscopy (XPS) (Thermo Fisher Scientific K-Alpha+). The Raman signal was detected by a nanoparticle Raman spectrometer (RAM-ANtouch), which have an operating wavelength of 532 nm, laser power of 1 mW, exposure time of 1 s and integration times of 1 time. All measurements were performed at room temperature.

3. Results and discussion

3.1. Structural and properties

Fig. 2(a-d) show the AFM images of the samples before and after thermal treatment. The as-deposited sample shows uniform, smooth and dense surface morphology, and the root mean square (RMS) surface roughness value is only 1.35 nm. The surface of the as-annealed samples were aggregated to form different sizes of islands or spikes. The RMS surface roughness value of the S3 sample is about 20 nm which is the highest one among these samples, and the RMS surface roughness value of the other samples are 9.29 nm (S2) and 14.6 nm (S3), respectively. In order to further explore the surface morphology of the samples, we carried out SEM measurements on the samples respectively, and the results are shown in Fig. 2(e-h). It can be seen from the figures that the surface morphology of the samples before and after annealing has changed significantly, and fine particles were formed on the surface after annealing, which may be the result of the oxidation of metallic Mo. As the annealing temperature increases, the number of particles gradually increases, which means that the surface roughness of the samples also increases. However, when we increased the annealing temperature to 300 ℃, the surface of the sample was almost completely covered by particles, formed a relatively dense oxide layer, which is exactly consistent with the decreased RMS surface roughness in Fig. 2(d). It shows that thermal treatment plays an important role in changing the surface morphology of the film, the higher the temperature, the more thermal energy is generated, so the more small particles formed by the film aggregation.

Fig. 3(a) shows the XRD patterns of the samples. Some weak diffraction peaks can be observed in the figure, because the film thickness were too thin, mainly showed the amorphous phase [20], but with the increase of the annealing temperature, the intensity of the diffraction peaks of the samples increase continuously. The diffraction peaks of S4 sample at 23.34°, 25.69°, 25.88°, 27.34° and 38.56° correspond to the (110), (040), (120), (021) and (131) crystal planes of the standard card (JCPDS No.35–0609). This is because the high temperature during thermal treatment caused the surface atoms to rearrange and became ordered to evolve into a crystalline state [21,22]. Moreover, thermal treatment was carried out in the ambient conditions, and the participation of oxygen promoted the formation of molybdenum oxide. Fig. 3 (b) is the absorption spectrum of the samples, which is mainly used to compare the absorption characteristics of the sample before and after thermal treatment. No obvious absorption band was observed in the as-deposited sample, but broad absorption band were observed in the range of 400 − 1000 nm in the as-annealed samples. The absorption of the as-annealed samples are enhanced overall. This can be attributed to the formation of oxygen defects, a large number of free electrons were adsorbed around the oxygen defects, resulting in the localized surface plasmon resonance (LSPR) effect [23]. With the increase of annealing temperature, the absorption intensity of the samples in the visible and near infrared-regions was enhanced, and this change may be related to the concentration of oxygen defects [15].

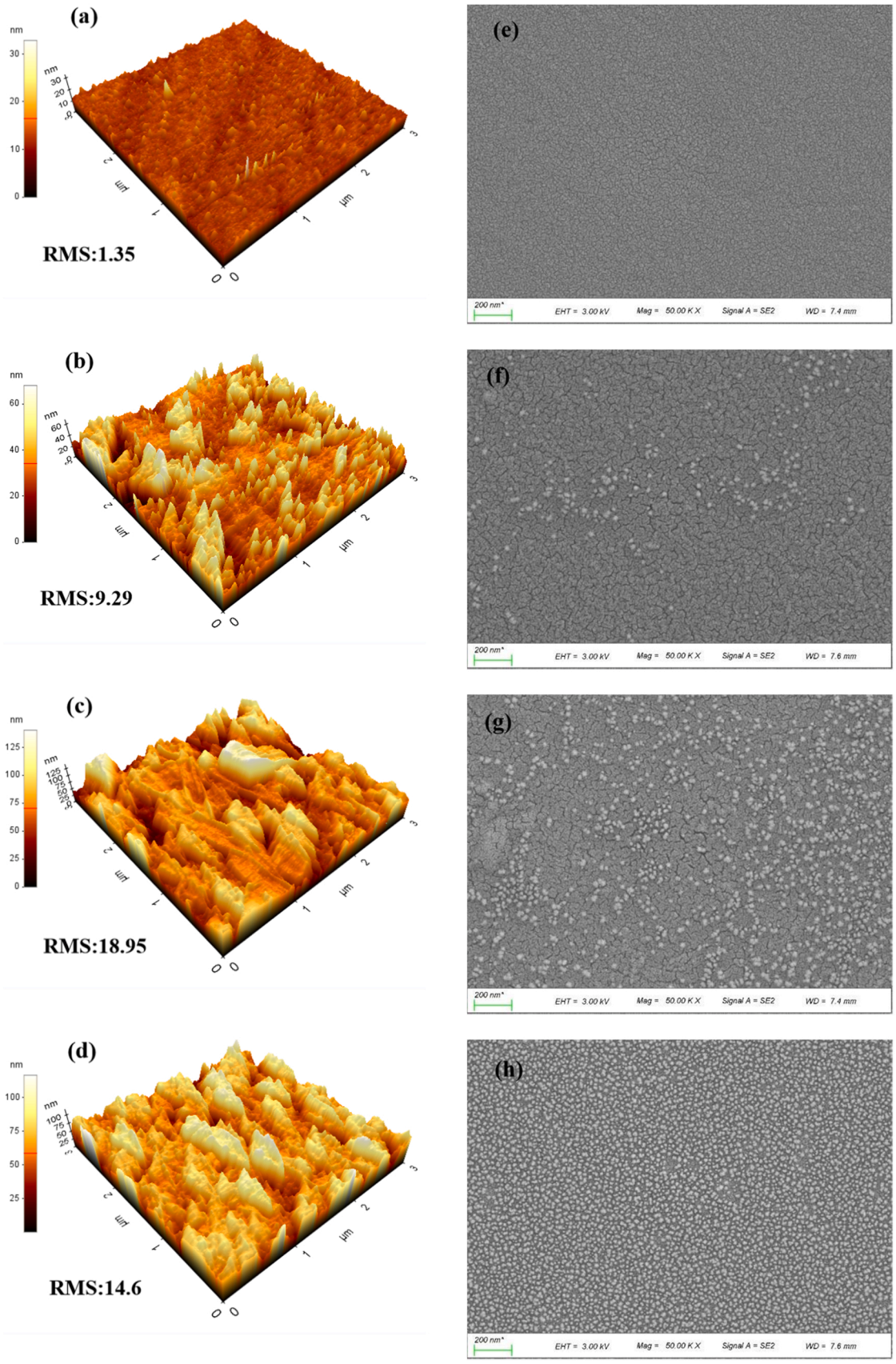

Fig. 2. AFM 3D images of (a) S1, (b)S2, (c)S3, (d)S4; SEM images of (e)S1, (f)S2, (g)S3, (h)S4.

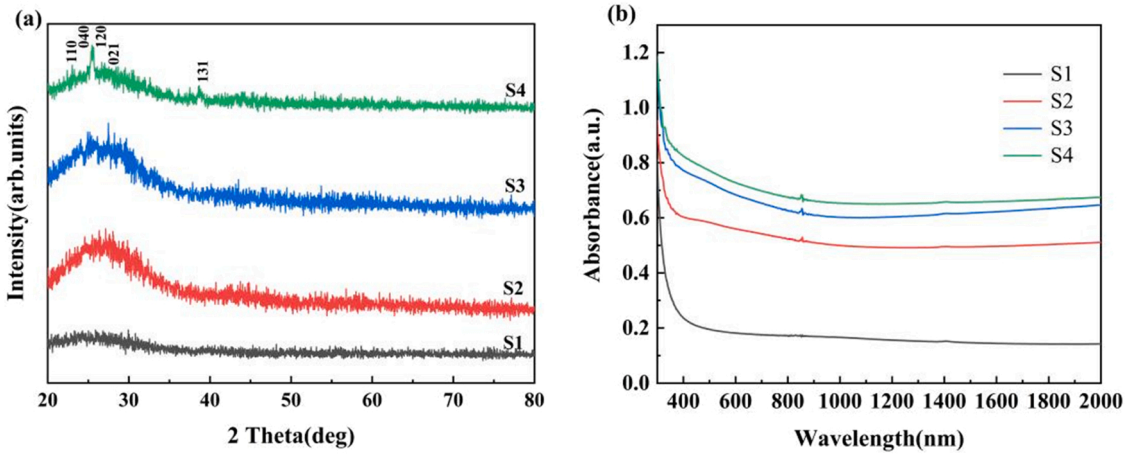

Fig. 3. The XRD pattern (a) and absorption spectra (b) of the samples.

We used XPS to further analyze the composition of MoO_{3-x}, as shown in Fig. 4. The obtained data were first corrected using the surface contamination C 1s (284.8 eV) as the standard. Fig. 4(a), (c), (e) show the Mo 3d XPS measurement spectra of samples S2, S3, S4, respectively. The double peaks in the figures are the Mo $3d_{5/2}$ and $3d_{3/2}$ energy levels formed by the spin-orbit splitting of Mo 3d energy levels, with an energy difference of 3.1 eV. This double peak can be fitted by two pairs of double peaks, corresponding to the mixed valence state of molybdenum. The characteristic peaks at 232.75 eV and 235.8 eV are corresponded to $3d_{5/2}$ and $3d_{3/2}$ of Mo^{6+}, and the characteristic peaks at 231.73 eV and 234.64 eV are corresponded to $3d_{5/2}$ and $3d_{3/2}$ of Mo^{5+} [24,25]. The existence of the characteristic peaks of Mo^{5+} is attributed to the formation of oxygen defects [26]. In Fig. 4(b), (d), (f), a broad asymmetric peak appears, which can be well fitted by three peaks. The characteristic peaks at 530.44 eV and 532.43 eV can be attributed to lattice oxygen and surface oxygen, respectively, while the characteristic peak at 531.1 eV can be attributed to oxygen defects [18,27]. When the annealing temperature rises, the oxygen defect content increases greatly but is begins to decrease with the further increase of temperature. When the annealing temperature is 250 ℃, the oxygen defect ratio is the highest. It shows that proper annealing temperature helps to increase the proportion of oxygen defects in metal oxide substrates. The above analysis is consistent with the results of optical analysis, which proves that there were free electrons around the oxygen defects, resulting in a wide absorption band.

3.2. SERS Property of MoO_{3-x} Substrate

In order to study the SERS performance of MoO_{3-x} thin films, we used methylene blue dye with a concentration of 10^{-4} mol/L as the probe molecule and a 532 nm laser as the excitation light source. As shown in Fig. 5(a), the peak of 447 cm^{-1} is attributed to the C-N-C skeletal deformation mode, and the significant peaks at around 1394 cm^{-1} and 1623 cm^{-1} corresponded to the C-N symmetrical stretching and C-C ring stretching, respectively [28]. The as-deposited Mo film shows a weak signal at 1623 cm^{-1}. After thermal treatment at different temperatures, the S2-S4 samples exhibit stronger Raman signals than that of the as-deposited sample [29]. Among them, the Raman signal of the S3 sample is the strongest, which is 6 times higher than that of the as-deposited sample. Correspondingly, the content of oxygen defects in XPS analysis is the highest, which we believe is the result of the combined action of a large number of free electrons brought by oxygen defects and the introduction of new surface states [15,24,30]. We selected the S3 sample for further study to explore its detection sensitivity. As shown in the Fig. 5(b), with the decrease of MB concentration, a weak signal can still be observed when the concentration is as low as 5×10^{-7} mol/L. Because the EF value is a powerful evaluation of SERS enhancement, we calculated the EF value of the samples at 1623 cm^{-1} according to the following formula:

$$EF = \frac{I_{SERS}/C_{SERS}}{I_0/C_0}$$

Here, I_{SERS} indicates the Raman intensity of 5×10^{-7} mol/L MB on MoO_{3-x} samples, and I_0 indicates the Raman intensity of 1×10^{-4} mol/L MB on blank K9. C_{SERS} and C_0 indicate the corresponding MB concentration. Fig. 5(c) shows the Raman intensity of I_{SERS} and I_0. After calculation, the EF value is as high as 1.06×10^4.

For an excellent SERS substrate, high uniformity is a very important parameter. Therefore, we randomly selected 20 points in the S3 sample for testing, and the results are shown in Fig. 5(e). In addition, we calculated the relative standard deviations (RSD) of Raman intensities at 447 cm^{-1}, 1393 cm^{-1}, 1623 cm^{-1}, which are 13.6 %, 14.4 %, and 13.4 %, respectively. The calculated results shown in Fig. 5(d) are all less than 15 %, indicating that the prepared MoO_{3-x} SERS substrates had relatively good uniformity. Likewise the stability of the substrate is also a very critical parameter in practical applications. As shown in Fig. 6(a), after being stored in the natural environment for 120 days, the measured spectrum still has a good performance. It can be seen from Fig. 6(b) that the intensity after 120 days is still about 70 % of the initial intensity, and the peak position is almost undisturbed. The results show that the MoO_{3-x} SRES substrate has long-term stability.

At present, there are two primary mechanisms of SERS enhancement of metal oxide substrates are generally accepted, they are electromagnetic enhancement mechanism (EM) and Chemical enhancement mechanism (CM) [8,31,32]. We simulated the electric field distribution of the samples using finite-difference-time-domain (FDTD) simulations, as shown in Fig. 7(a–d). The 532 nm laser was irradiated vertically and polarized along the y-axis. The as-deposited sample is dense and homogeneous, so the electric field strength is weak. The as-annealed samples formed particles with a diameter of about 20 nm, and the roughness increased to a certain extent. With the increase of roughness, the electric field strength also increases. When the annealing

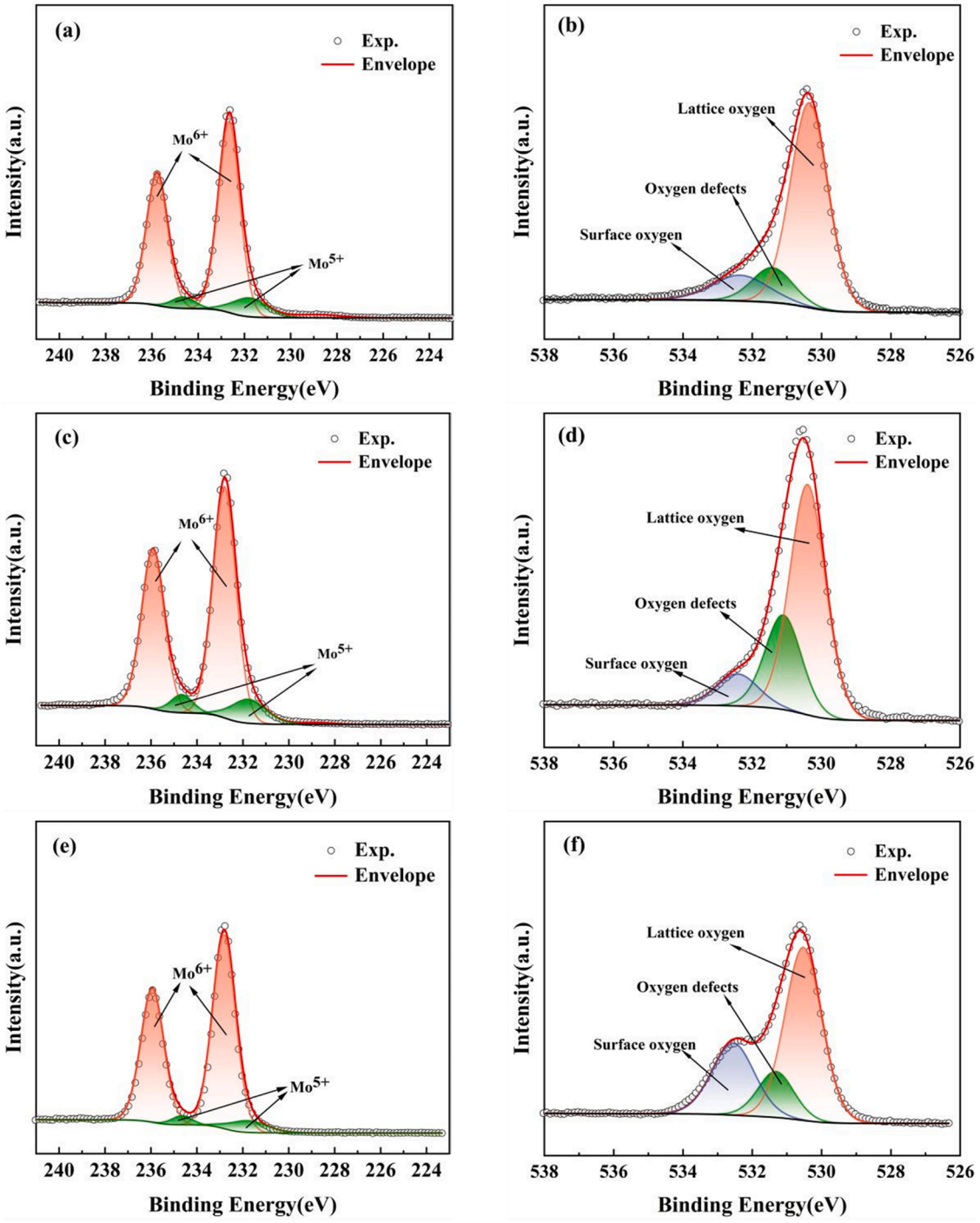

Fig. 4. The XPS spectrum of Mo 3d for (a)S2, (c)S3, (e)S4 and O 1 s for (b)S2, (d)S3, (f)S4.

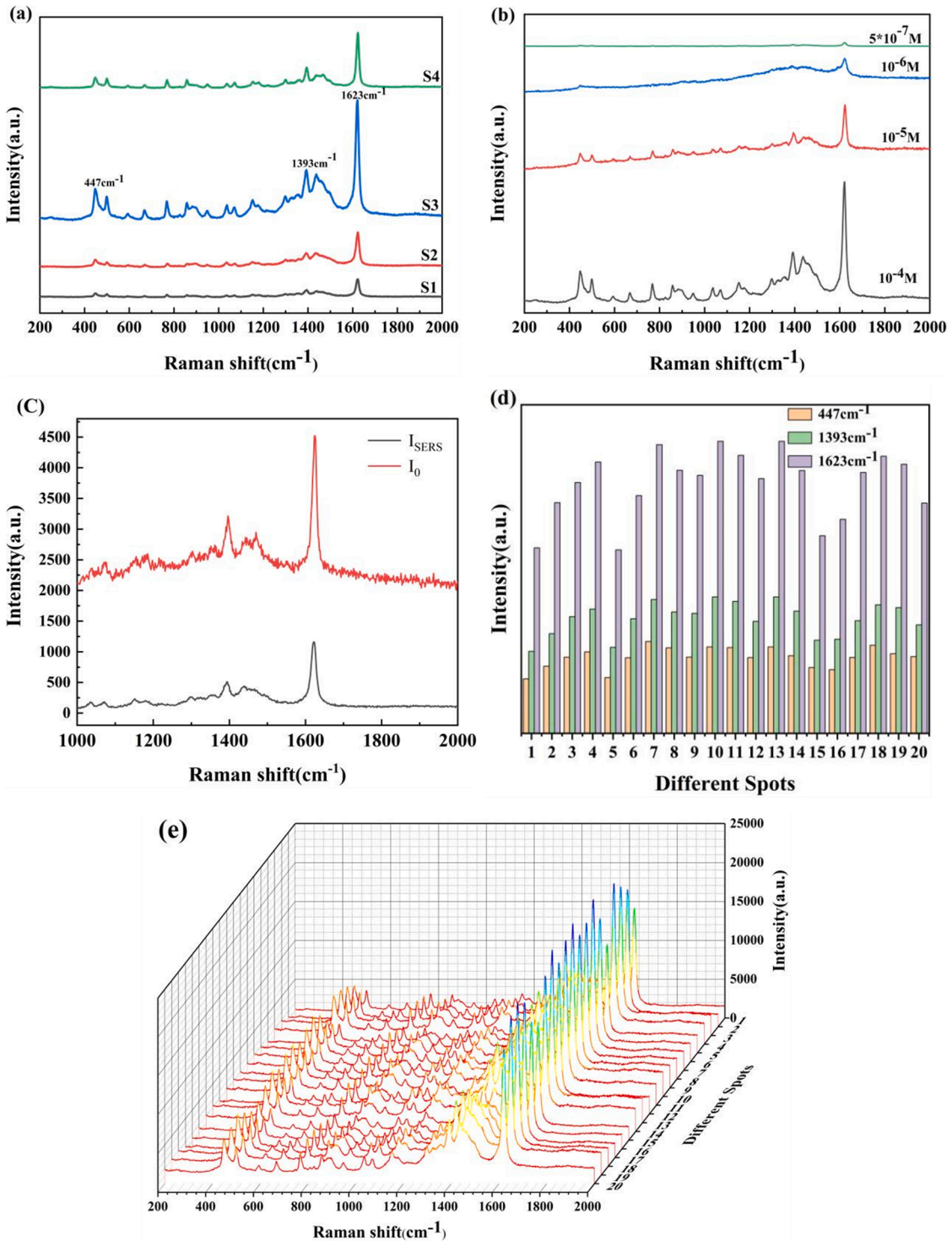

Fig. 5. (a) SERS spectra of MB (10^{-4} mol/L) on different substrates; (b) SERS spectra of MB with varying concentrations of 10^{-7}-10^{-4} mol/L on the sample S3; (c) the Raman intensity of I_{SERS} and I_0; (d) the corresponding RSD values of characteristic peaks at 1623 cm^{-1}, 1393 cm^{-1}, and 447 cm^{-1}; (e) SERS spectra of MB (10^{-4} mol/L) collected from 20 random sites on the sample S3.

temperature reaches 250 °C, the roughness reaches the maximum, and the electric field strength also reaches the maximum. With the further increase of the temperature, both the roughness and the electric field strength show a downward trend. The simulation results are highly consistent with the experimental results. Oxygen defects also play an irreplaceable role in chemical enhancement, which effectively enhances Raman scattering by introducing new surface states that provide a large number of photo-induced charge transfer (PICT) processes [33]. The schematic diagram shown in Fig. 8, The VB and CB of molybdenum trioxide are −7.36 eV and −4.26 eV, respectively [18], and a new valence band is generated below CB due to the introduction of oxygen defects [19,28]. The HOMO and LUMO of MB are −5.67 eV and −3.81 eV, respectively [34]. The enhancement mechanism under the excitation of 532 nm laser includes exciton resonance (μ_{CR}) of MoO_{3-x} defect state and photo-induced charge transfer (μ_{PICT}) between MoO_{3-x} and MB molecules [28,35].

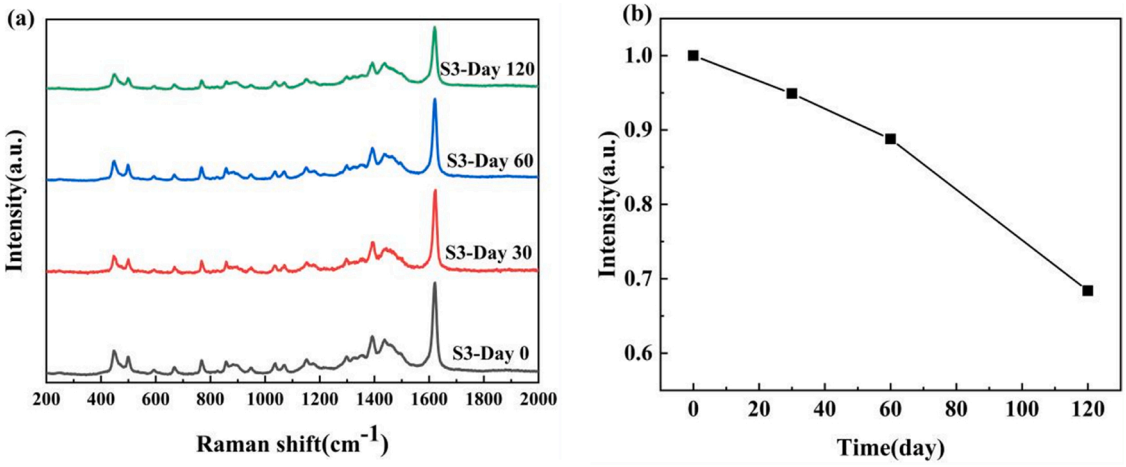

Fig. 6. (a)SERS spectra of MB on S3 substrate and (b) Raman intensity ratio of S3 sample at 1623 cm^{-1} before and after storing in air up to 120 days.

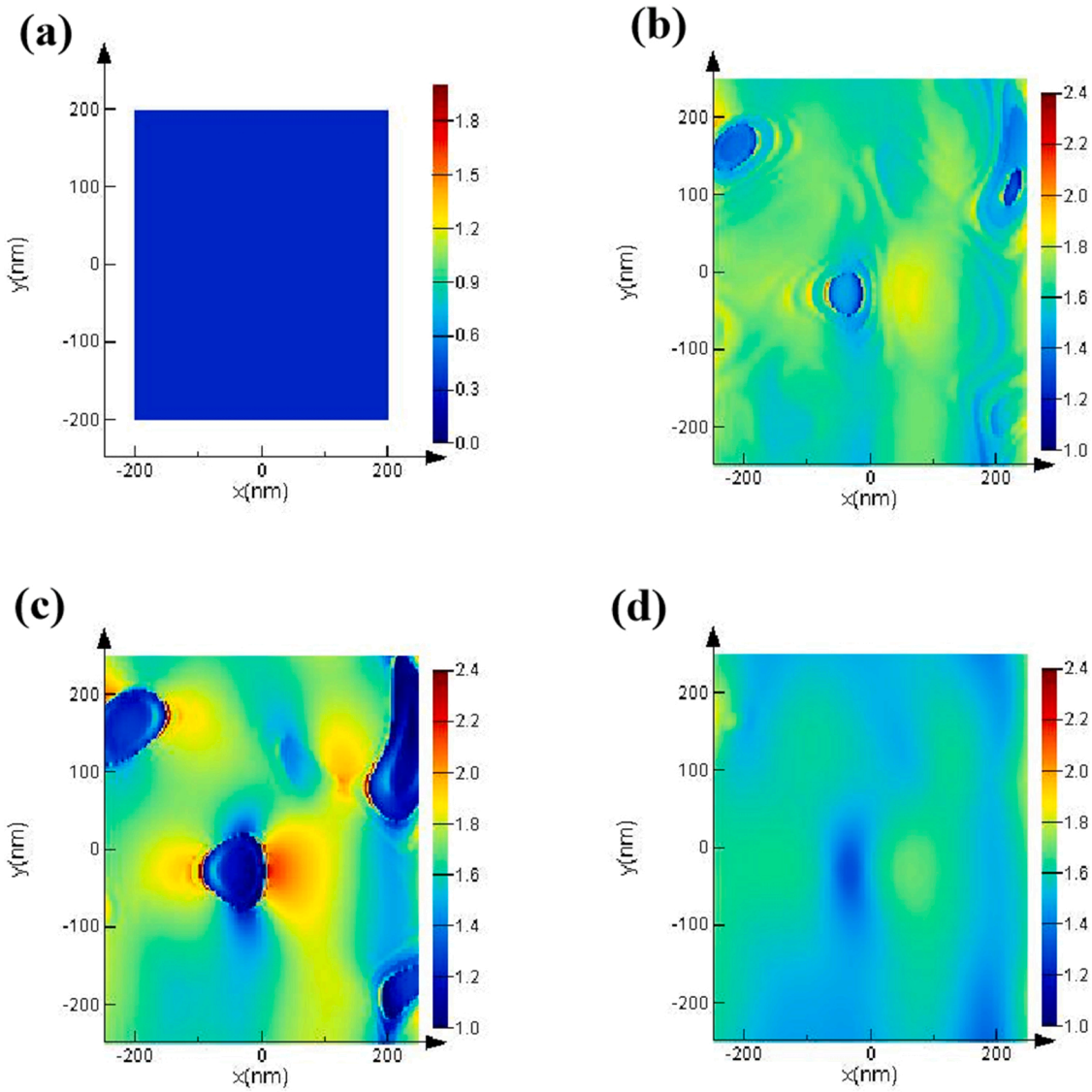

Fig. 7. FDTD simulation patterns of patterns of electric field amplitude for (a) S1, (b) S2, (c) S3 and (d) S4.

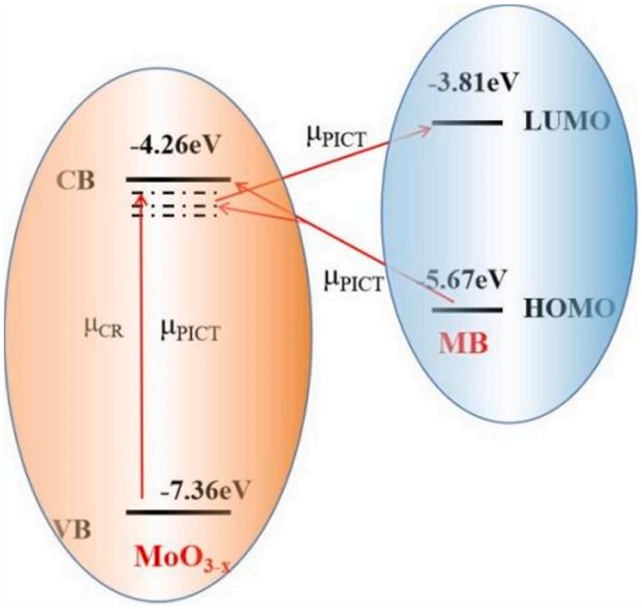

Fig. 8. The schematic representation of energy-level diagram.

4. Conclusions

In conclusion, we successfully prepared MoO_{3-x} SERS substrates with different contents of oxygen defects by adjusting annealing temperature. Compared to that of noble metal materials, the MoO_{3-x} substrates exhibited good stability, uniformity and with the detection limit is 5×10^{-7} mol/L. Raman scattering signal intensity from metal oxide substrates is greatly enhanced by the combined effect of the electromagnetic enhancement caused by the LSPR effect, and the chemical enhancement of coupled resonance and charge transfer provided by the new surface states.

Declaration of Competing Interest

The authors declare that they have no known competing financial interests or personal relationships that could have appeared to influence the work reported in this paper.

Data Availability

No data was used for the research described in the article.

Acknowledgment

This work was supported by the National Natural Science Foundation of China (61775141, 62075133, and 62275159).

References

[1] D.-W. Li, W.-L. Zhai, Y.-T. Li, Y.-T. Long, Recent progress in surface enhanced Raman spectroscopy for the detection of environmental pollutants, Microchim. Acta 181 (2013) 23–43.
[2] X.M. Qian, S.M. Nie, Single-molecule and single-nanoparticle SERS: from fundamental mechanisms to biomedical applications, Chem. Soc. Rev. 37 (2008) 912–920.
[3] V. Sharma, V. Krishnan, Fabrication of highly sensitive biomimetic SERS substrates for detection of herbicides in trace concentration, Sens. Actuators B: Chem. 262 (2018) 710–719.
[4] Y. Sun, P. Peng, R. Guo, H. Wang, T. Li, Exonuclease III-boosted cascade reactions for ultrasensitive SERS detection of nucleic acids, Biosens. Bioelectron. 104 (2018) 32–38.
[5] W.J. Cho, Y. Kim, J.K. Kim, Ultrahigh-density array of silver nanoclusters for SERS substrate with high sensitivity and excellent reproducibility, ACS Nano 6 (2012) 249–255.
[6] A. Liu, G. Wang, F. Wang, Y. Zhang, Gold nanostructures with near-infrared plasmonic resonance: synthesis and surface functionalization, Coord. Chem. Rev. 336 (2017) 28–42.
[7] X. Wang, C. Wang, L. Cheng, S.T. Lee, Z. Liu, Noble metal coated single-walled carbon nanotubes for applications in surface enhanced Raman scattering imaging and photothermal therapy, J. Am. Chem. Soc. 134 (2012) 7414–7422.
[8] S.Y. Ding, E.M. You, Z.Q. Tian, M. Moskovits, Electromagnetic theories of surface-enhanced Raman spectroscopy, Chem. Soc. Rev. 46 (2017) 4042–4076.
[9] J. Krajczewski, A. Kudelski, Shell-isolated nanoparticle-enhanced Raman spectroscopy, Front Chem. 7 (2019) 410.
[10] S.-Y. Ding, J. Yi, J.-F. Li, B. Ren, D.-Y. Wu, R. Panneerselvam, Z.-Q. Tian, Nanostructure-based plasmon-enhanced Raman spectroscopy for surface analysis of materials, Nature Reviews, Materials 1 (2016).
[11] X.X. Han, W. Ji, B. Zhao, Y. Ozaki, Semiconductor-enhanced Raman scattering: active nanomaterials and applications, Nanoscale 9 (2017) 4847–4861.
[12] Z.-Q. Tian, B. Ren, D.-Y. Wu, Surface-enhanced Raman scattering: from noble to transition metals and from rough surfaces to ordered nanostructures, The, J. Phys. Chem. B 106 (2002) 9463–9483.
[13] W. Ji, B. Zhao, Y. Ozaki, Semiconductor materials in analytical applications of surface-enhanced Raman scattering, J. Raman Spectrosc. 47 (2016) 51–58.
[14] Y.F. Chan, H.J. Xu, L. Cao, Y. Tang, D.Y. Li, X.M. Sun, ZnO/Si arrays decorated by Au nanoparticles for surface-enhanced Raman scattering study, J. Appl. Phys. 111 (2012).
[15] S. Cong, Y. Yuan, Z. Chen, J. Hou, M. Yang, Y. Su, Y. Zhang, L. Li, Q. Li, F. Geng, Z. Zhao, Noble metal-comparable SERS enhancement from semiconducting metal oxides by making oxygen vacancies, Nat. Commun. 6 (2015) 7800.
[16] Q. Zhang, X. Li, W. Yi, W. Li, H. Bai, J. Liu, G. Xi, Plasmonic MoO2 nanospheres as a highly sensitive and stable non-noble metal substrate for multicomponent surface-enhanced Raman analysis, Anal. Chem. 89 (2017) 11765–11771.
[17] Y. Cao, P. Liang, Q. Dong, D. Wang, Zhang, L. Tang, L. Wang, S. Jin, D. Ni, Z. Yu, Facile reduction method synthesis of defective MoO2- x nanospheres used for SERS detection with high chemical enhancement, Anal. Chem. 91 (2019) 8683–8690.
[18] Z. Zheng, S. Cong, W. Gong, J. Xuan, G. Li, W. Lu, F. Geng, Z. Zhao, Semiconductor SERS enhancement enabled by oxygen incorporation, Nat. Commun. 8 (2017) 1993.
[19] H. Wu, H. Wang, G. Li, Metal oxide semiconductor SERS-active substrates by defect engineering, Analyst 142 (2017) 326–335.
[20] R. Hong, W. Shao, W. Sun, C. Deng, C. Tao, D. Zhang, Laser irradiation induced tunable localized surface plasmon resonance of silver thin film, Opt. Mater. 77 (2018) 198–203.
[21] J.V.B. Moura, J.V. Silveira, J.G. da Silva Filho, A.G. Souza Filho, C. Luz-Lima, P.T. C. Freire, Temperature-induced phase transition in h-MoO3: stability loss mechanism uncovered by Raman spectroscopy and DFT calculations, Vib. Spectrosc. 98 (2018) 98–104.
[22] X. Fan, G. Fang, P. Qin, N. Sun, N. Liu, Q. Zheng, F. Cheng, L. Yuan, X. Zhao, Deposition temperature effect of RF magnetron sputtered molybdenum oxide films on the power conversion efficiency of bulk-heterojunction solar cells, J. Phys. D: Appl. Phys. 44 (2011).
[23] X. Tan, L. Wang, C. Cheng, X. Yan, B. Shen, J. Zhang, Plasmonic MoO3-x@MoO3 nanosheets for highly sensitive SERS detection through nanoshell-isolated electromagnetic enhancement, Chem. Commun. (Camb.) 52 (2016) 2893–2896.
[24] M.T. Greiner, L. Chai, M.G. Helander, W.-M. Tang, Z.-H. Lu, Metal/metal-oxide interfaces: how metal contacts affect the work function and band structure of MoO3, Adv. Funct. Mater. 23 (2013) 215–226.
[25] B. Yang, Y. Chen, Y. Cui, D. Liu, B. Xu, J. Hou, Over 100-nm-thick MoOx films with superior hole collection and transport properties for organic solar cells, Adv. Energy Mater. 8 (2018).
[26] S.R. Hammond, J. Meyer, N.E. Widjonarko, P.F. Ndione, A.K. Sigdel, A. Garcia, A. Miedaner, M.T. Lloyd, A. Kahn, D.S. Ginley, J.J. Berry, D.C. Olson, Low-temperature, solution-processed molybdenum oxide hole-collection layer for organic photovoltaics, J. Mater. Chem. 22 (2012).
[27] M.K. Patil, S.H. Gaikwad, S.P. Mukherjee, Phase- and morphology-controlled synthesis of tunable plasmonic MoO3–x nanomaterials for ultrasensitive surface-enhanced Raman Spectroscopy detection, J. Phys. Chem. C 124 (2020) 21082–21093.
[28] C. Li, Y. Huang, K. Lai, B.A. Rasco, Y. Fan, Analysis of trace methylene blue in fish muscles using ultra-sensitive surface-enhanced Raman spectroscopy, Food Control 65 (2016) 99–105.
[29] M. Anwar, C.A. Hogarth, R. Bulpett, Effect of substrate temperature and film thickness on the surface structure of some thin amorphous films of MoO3 studied by X-ray photoelectron spectroscopy (ESCA), J. Mater. Sci. 24 (1989) 3087–3090.
[30] J. Lin, Y. Shang, X. Li, J. Yu, X. Wang, L. Guo, Ultrasensitive SERS detection by defect engineering on single Cu2 O superstructure particle, Adv. Mater. 29 (2017).

[31] M.F. Cardinal, E. Vander Ende, R.A. Hackler, M.O. McAnally, P.C. Stair, G. C. Schatz, R.P. Van Duyne, Expanding applications of SERS through versatile nanomaterials engineering, Chem. Soc. Rev. 46 (2017) 3886–3903.
[32] J.R. Lombardi, The theory of surface-enhanced Raman scattering on semiconductor nanoparticles; toward the optimization of SERS sensors, Faraday Discuss. 205 (2017) 105–120.
[33] C. Gu, D. Li, S. Zeng, T. Jiang, X. Shen, H. Zhang, Synthesis and defect engineering of molybdenum oxides and their SERS applications, Nanoscale 13 (2021) 5620–5651.
[34] L.C. Sim, K.H. Leong, S. Ibrahim, P. Saravanan, Graphene oxide and Ag engulfed TiO2 nanotube arrays for enhanced electron mobility and visible-light-driven photocatalytic performance, J. Mater. Chem. A 2 (2014) 5315–5322.
[35] B. Yang, Y. Wang, S. Guo, S. Jin, E. Park, L. Chen, Y.M. Jung, Charge transfer study for semiconductor and semiconductor/ metal composites based on surface-enhanced Raman scattering, Bull. Korean Chem. Soc. 42 (2021) 1411–1418.